

Study of impurity distribution in mechanically polished, chemically treated and ultra-high vacuum degassed pure Niobium samples using TOFSIMS technique

A. Bose ^a, S. C. Joshi ^a

^a Proton Linac and Superconducting Cavities Division

Raja Ramanna Centre for Advanced Technology, Indore, M. P. 452013, India

Abstract

The performance of Superconducting radio frequency cavities (SCRF) are highly dependent on the surface treatment processes, which in turn is influenced by the chemistry within the penetration depth of Niobium (Nb). The present study analyses various impurities within the RF penetration depth (~50nm) of Nb samples treated by SCRF cavity processing techniques like colloidal silica polishing (simulating centrifugal barrel polishing), buffer chemical polishing (BCP), high pressure rinsing (HPR) and degassing under ultra high vacuum (UHV) condition at 600°C for 10hrs. Various modes of Time of flight secondary ion mass spectrometry (TOFSIMS) technique was employed to study the effect of the above treatments on the vast spectrum of impurities that include interstitials, hydrocarbons, oxides, acidic residuals, reaction products and metallic impurities. UHV degassing treatment was the only treatment capable of reducing hydrogen contamination, but, it led to extensive oxygen, carbon and metallic impurities in the bulk Nb. BCP treated samples, on the other hand exhibited minimum hydrocarbon and metallic contamination along with thinnest oxide layer at ~2.7nm. But, BCP treatment led to extensive contamination of the oxide layer with residuals and reaction products of acids used in BCP solution. HPR treatment, on the other hand was effective in reducing the acidic impurities on the top surface. The study confirms that impurity distribution in Nb is not only sensitive to the surface treatment, but also to their sequence. This study can be further extended to other surface treatments which would help in evolving SCRF cavity processing techniques.

Key words

TOFSIMS; Buffer chemical polish (BCP); High pressure rinse (HPR); UHV degassing; NbH_x; impurity.

1. Introduction

Superconducting radio frequency (SCRF) cavities made out of high purity niobium (Residual resistivity ratio, RRR ~ 300) is the primary choice for the next generation linear accelerators (Linac). Research and development activities for building a 1 GeV superconducting linac (Indian spallation neutron source) has been initiated at RRCAT, Indore [1]. The medium energy section of this linac would consist of 650 MHz SCRF cavities made from Nb. The optimized target gradient of these types of cavities would be ~ 19 MV/m [2]. These cavities would undergo various chemical and thermal treatments to improve their accelerating gradient at a proposed quality factor (Q_0) of $\sim 10^{10}$. Since large numbers of cavities are required to build a superconducting accelerator, so these treatments should also ensure repeatability in their performance. The performance of these cavities have been found to depend on the surface treatments, and its sequence. For example, the average accelerating gradient of 1.3GHz electropolished (EP) cavities were $\sim 15\%$ higher than buffer chemical polished (BCP) cavities [3]. Moreover, additional low temperature baking, improves the gradient and Q_0 in EP as well as BCP treated cavities [4]. But, in some exceptional cases, stand-alone BCP treated 1.3GHz cavities have also reached 40MV/m, which adds complexity to the above subject [5]. It was also found that, if the phosphoric acid in BCP solution is replaced with sulphuric acid, the Q-slope improves in comparison to standard BCP treated cavity [5]. These factors presents before us, the challenges, in understanding the effects of treatments on the cavity performance. The primary effect of these treatments is to alter the impurities within the RF penetration depth of Nb, which is close to ~ 50 nm [6]. Hence, the role of impurities in inducing variation in cavity performance assumes importance; which forms the basis of present research. The motivation to analyze the impurities among host of other factors would be presented in the subsequent paragraphs.

Various forms of impurities, that include interstitials [7-8], metallic, non-metallic [9-10], oxides [10-12]; combined with their locations that includes surface [9, 10, 13, 14, 15], subsurface [7, 8, 12], inside penetration depth [7, 11], bulk [4] and grain boundaries [16-17]; have been directly or indirectly linked to the cavity performance [7-17]. For example surface impurities such as sulfur [9,18], aluminium [9], fluorine [18], chlorine [15] and carbon [16, 18, 19] have been found on EP and/or BCP treated surfaces which are potential sources of field emission (FE) [9, 16, 18] and degrades the cavity performance [14, 19-20]. Additionally, investigation of FE created craters has revealed the presence of many non-metallic and metallic impurities [15]. Moreover, multipacting was found to be enhanced due to adsorbates or condensed gas [14]. On the other hand, degrading effect of interstitial impurities like H, O is well known in SCRF community. Moreover superconducting parameters like critical temperature (T_c), the upper critical field (H_{c2}) [21], surface superconductivity [13] and residual resistance [14] of Nb are in many ways affected by impurities which in turn might affect the maximum gradient and the Q-slope. It has also been suggested that adsorbed or surface chemical impurities may have magnetic moments that can create normal conducting states within Δ , thereby reducing T_c [22]. In fact the suspected roles of impurities like N, C, F, P, S, $C_xH_y(OH)_z$ and some niobium sub oxides have also been proposed [13].

Hence, it can be proposed that a vast spectrum of impurities/ contaminants may be responsible for variation in SCRF cavity performance. To understand the role of each SCRF processing treatment on the total spectrum of impurities, Time of flight secondary ion mass spectrometer (TOF-SIMS 5 from M/s IONTOF, GmbH) was selected as the surface analytical tool. Numerous SIMS studies have been carried out earlier to analyze the niobium

surface. Of them, few studies have focused on the oxide layer development against oxygen exposure [23-24], while others have proposed mechanism to investigate the oxide composition [25-26]. Studies using SIMS has also concentrated on the changes due to ultra-high vacuum thermal degassing and low temperature baking treatment on the oxide layer and interstitial impurities like H, C, O and N [7, 27]. But, there has been a very limited emphasis to understand the step-wise effect of each surface treatment on the vast spectrum of impurities that include interstitials, hydrocarbons, oxides, acidic residual, reaction products and metallic impurities of Nb. Analysis of few impurities have been carried out using techniques like XPS [28], AES [29], ERDA [8] and few more. But the coverage of TOFSIMS technique being large along with simultaneous detection of all species, ensures analysis with greater details, which can be complemented with the results from other instruments.

The present study investigates the changes in the impurity distribution within the penetration depth of Nb due to sequential treatments of colloidal silica polishing (CSP), BCP, high pressure rinsing (HPR) and thermal degassing treatment. The work also tries to relate the sputtered ionic species from SIMS analysis with various impurities that were present inside Nb. The purpose of choosing CSP as baseline treatment stems from two factors. First, the surface condition of the samples cut from the raw Nb sheets was not known. Second, colloidal silica polishing is the proposed polishing step in centrifugal barrel polishing treatment prior to chemical treatments to cavities being processed at RRCAT. Finally selection of BCP treatment was based on two prime reason. First, BCP treated 650MHz cavities have shown encouraging results at JLab [30] and second is the rise of large grain cavities. However, this study presented here would also help in analyzing the complex EP process in future which has more variables like voltage, temperature, anode cathode ratio, anode cathode distance etc.

2. Experimental

2.1. Materials

In this work four high purity Niobium samples P78, P79, P115 and P117 of 13mm x 8mm (approx.) sizes, were cut from polycrystalline niobium sheet (2.8mm thick) procured from M/s Plansee GmbH. The physical properties and chemical composition of the niobium samples are mentioned in table 1.

Table 1:Chemical composition and grain size of the niobium used for our analysis

Material Source	RRR	Grain size	Composition (wt. ppm)							
			H	C	N	O	Ta	Fe	Cr	W
M/s Plansee, GmbH	495	80 μ m	8	10	10	40	83	<6	<0.1	1.07

2.2. Preparation

The samples were initially ultrasonically cleaned in micro-90 detergent solution followed by ultrasonic cleaning in ultra-pure water (UPW). The step-wise treatments on two sets of samples (P78 and P79) are listed in table 2. Each of these treatments focused on following the SCRF cavity processing sequence. The colloidal silica polished samples named as P78C and P79C, were initially rough polished by silicon carbide papers and fine polished using diamond paste, followed by colloidal silica polishing using 40 nm silica solutions procured from M/s Allied high Tech., USA. These samples were then rinsed ultrasonically in micro-90 solution followed and UPW for 30 minutes each, which were subsequently analyzed using TOFSIMS technique. After analysis, the samples (P78C and P79C) were BCP treated for at least 60 minutes in a fresh acid mixture of HF: HNO_3 : H_3PO_4 (1:1:2), stirred at a constant speed using teflon coated magnetic stirrer. The solution was surrounded by ice-water mixture that maintained the

acid temperature within 11 °C to minimize hydrogen uptake [31]. The temperature was continuously monitored using a Teflon coated thermocouple. BCP treated samples were ultrasonically rinsed in UPW for 60 minutes and identified as P78B and P79B, which were subsequently analyzed. The average etching rate was ~0.65 $\mu\text{m}/\text{min}$. Finally, they were high pressure rinsed (HPR) using a sample holder arrangement in HPR assembly inside class 100 clean room, at a pressure of 85 kg/cm^2 at a distance of ~10 cm for 10 minutes. These samples were identified as P78H and P79H.

Another two sets of sample P115 and P117 were BCP treated and CS polished respectively. These samples were analyzed and subsequently annealed at 600 °C for 10hrs in high vacuum annealing furnace (< 2e-6 mbar) and identified as P115U and P117U. The purpose of these two samples was to investigate the effect of UHV degassing on impurity diffusion and changes in oxide layer. It was important to establish co-relation, if any, between the diffused impurities and the impurities that were left inside Nb, by previous treatments like BCP and CS.

Table 2: Treatment sequence of four Nb samples (P78, P79, P115, P117) used in present analysis

Steps	Treatment and its used abbreviation	Parameters/ Time	First Sample	Second Sample	Third sample	Fourth Sample
1(a)	Colloidal Silica polish	CS	40 nm Silica solution			
(b)	Ultrasonic cleaning in Micro-90	--	30 minutes	P78C	P79C	X P117C
(c)	Ultrasonic cleaning in ultra-pure water	UPW	30 minutes			
2(a)	Buffer chemical polish	BCP	1 hr at ~11°C			
(b)	Ultrasonic cleaning in ultra-pure water	UPW	1 hr	P78B	P79B	P115B X
3.	High pressure rinsing	HPR	10 min at 85 kg/cm^2 water pressure	P78H	P79H	X X
4.	UHV annealing	UHV	600°C for 10 hrs at <2e-6 mbar	X	X	P115U P117U

Processing and handling of all samples were done with extreme precaution to avoid any external contamination apart from the treatment step itself. After each treatment the sample surface were kept untouched and were loaded inside SIMS loadlock chamber (< 3e-7 mbar) within 30 minutes of the concerned preparation step (except P115).

The above procedure of treatments and analysis were repeated again on few Nb samples including sample from a different supplier and the results exhibited similar trend. Any variations that were observed have also been incorporated in the present article. However, to avoid too much data, the detailed reporting of the results related to other samples was avoided.

2.3. TOF-SIMS

The measurements using TOFSIMS technique were divided into three parts. Part 1 carried out impurity analysis of the top surface using Static SIMS technique; Part 2 was devoted to oxide layer analysis using slow sputtering technique and Part 3 performed impurity analysis throughout the penetration depth using dynamic SIMS technique.

The static SIMS spectrum of the two sets of samples (P78 and P79), after each treatment, were obtained in positive and negative secondary ion mode using a pulsed 30keV Bi_1^+ primary ion beam at ~2pA current, rastered over an area of 350 μm x 350 μm . To ensure analysis within the static limit, the primary ion dose was kept within 7e11ions/cm² by limiting the acquisition time to less than 80 seconds. The spectra were recorded at a minimum

of 3 fresh spots on each sample, to measure repeatability. The average value of three spots were used to compare the data between the above mentioned surface treatments. The detailed procedure of comparison shall be explained in section 3.1.

The second stage of analysis involved slow sputtering of the oxide layer using pulsed Bi_1^+ primary ion beam (30keV, ~4pA) alone for an extended period (>4000sec). The measurements were done on P78C, P78B, P78H and P115U to compare the oxide layer. The area for analysis was kept at 80 μm x 80 μm . To remove the edge effect after extended sputtering, the depth profile was reconstructed from the 50 μm central area using the TOFSIMS Surface lab software. Single spot was analyzed for each sample. It was ensured that the areas to be analyzed do not have any localized impurities; by observing the ion images in positive and negative mode prior to analysis. The ion images, prior to oxide depth profile, were acquired in both modes for 10 seconds of sputtering.

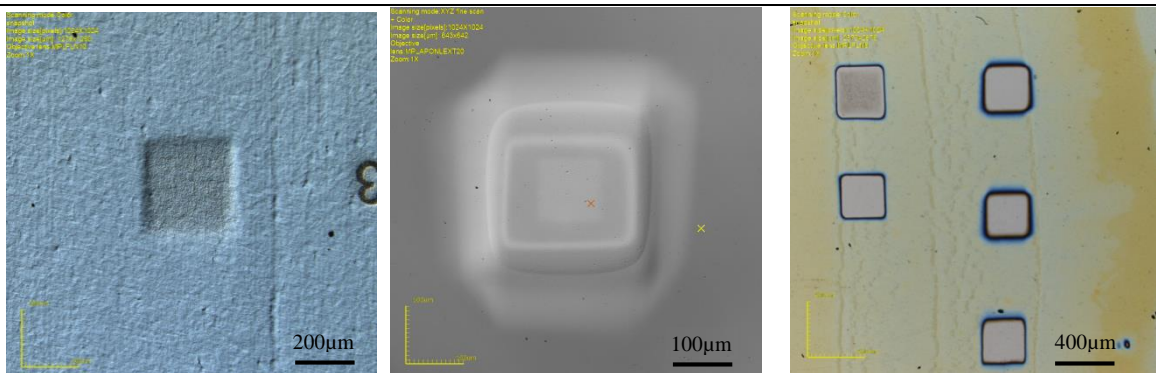


Figure 1: Few SIMS craters created by Cs^+ ions at 1kV in (a) Colloidal Silica polished Nb sample, (b) Nb Thin film (~470 nm) deposited on Si wafer and (c) Anodized Nb sample at 50 volt using 1:5 $\text{NH}_4\text{OH}:\text{H}_2\text{O}$ solution.

Finally the depth profile analysis up to the penetration depth of Nb was carried out in interlaced mode with pulsed Bi_1^+ at 30 keV as the analysis gun and low energy Cs^+ and O_2^+ as the sputter gun. Cs^+ ions at 1keV as sputter gun was used to analyze non-metallic impurities and oxides while O_2^+ gun at 500eV was applied for detection of metallic impurities. For all measurements, the sputter current for Cs^+ gun at 1keV and O_2^+ gun at 500eV was kept constant at ~ 74nA and ~100nA respectively. The area of analysis across all measurements was 100 μm x 100 μm inside the sputter area of 300 μm x 300 μm . The depth profiles are plotted in figure 7 and 11, where, X-axis represents time and Y-axis the normalized intensity. The normalization of the counts from negative ion fragments from each spot was done with Nb^- counts. This technique has been used previously [7]. However normalization process was performed only after the removal of the top oxide layer. This was done to eliminate the matrix effect arising due to the oxide layer. Moreover, Nb^- intensity was found to stabilize, only after the removal of oxide layer. The depth profile compares the impurities between all treatments listed in table 2. The average values between the two sets of samples (P78 and P79) was plotted for CS polishing, BCP treatment and subsequent HPR treatment which are mentioned as Avg(P78 79)C, Avg(P78,79)B and Avg(P78,79)H respectively. On the other hand average data of P115U and P117U were plotted for UHV degassed BCP treated and CS polished samples respectively. Time on the X-axis was converted to depth by estimating the sputter rate of the sputter gun. The sputter rate estimation requires the measurement of crater depth of Nb, which is difficult owing to its initial roughness, final crater roughness, sample slope combined with shallow depth created by low energy sputter gun. To overcome these difficulties 3 different types of samples were prepared. First sample was colloidal silica polished sample with a roughness of 21±13 nm. The second sample was a ~470 nm Nb thin film grown on Si

wafer and the third sample was a set of anodized niobium samples with varying oxide thicknesses, which were calculated on the basis of formula available in literature [32]. The optical images of a few such sample areas are shown in figure 1 along with their craters. The craters of first 2 samples were measured using 3-D confocal microscope and stylus instrument. In case of third sample SIMS sputtering was stopped as we reached bulk Nb. The sputter rate of Cs 1kV sputter gun was estimated to be 0.195 ± 0.03 nm/s from colloidal silica polished samples; 0.213 ± 0.001 nm/s (2 spots) for Nb thin film and 0.21 ± 0.031 nm/s estimated from anodized niobium oxide layers. However, the sputter rate of O_2^+ gun at 500eV was measured in the first two samples only. The average sputter rate was found to be 0.051 ± 0.04 nm/s.

The typical mass resolution was > 8000 at mass ^{28}Si for all measurements and vacuum level was less than $5e-10$ torr prior to all analysis. To the best of our knowledge we could not find such a detailed analysis which is critical to the understanding of the variability from various treatments applied on the SCRF cavities.

3. Results and discussions

The results and discussion part was divided in three sections. Section 3.1 analyzes the changes in impurities on the top monolayer using static SIMS approach, while section 3.2 extends the study to the top oxide layer using slow sputtering depth profiling approach with Bi_1^+ beam alone and finally section 3.3 reports the impurity analysis up to the penetration depth (~ 50 nm) using dual beam dynamic TOF-SIMS technique.

3.1 Top layer impurity analysis using Static SIMS

Figure 2 shows a typical positive and negative secondary ion spectra of BCP treated niobium (P78B) surface. The top surface of niobium was found to be covered by an oxide layer with an over layer of hydrocarbons indicated by the presence $C^{+/-}$, $CH^{+/-}$, $CH_2^{+/-}$ and host of other $C_xH_y^{+/-}$ and $C_xH_yO_z^{+/-}$ ion fragments. The hydrocarbons present over the top niobium oxide surface also emitted fragments like $H^{+/-}$, $H_2^{+/-}$, $NbH_x^{+/-}$, $NbC^{+/-}$, $NbCH_x^{+/-}$, $NbC_xH_y^{+/-}$, $NbC_xH_y^{+/-}$ and $NbO_xC_yH_z^{+/-}$. The top layer of BCP treated sample also emitted various fragments of acidic residues indicated by F^- , F_2^- , H_2F^- , P^- , PO^- , PO_2^- , PO_3^- , N^+ , $NO^{+/-}$, NOH^- , NO_2H^- , Cl^- as well as reaction products like $NbO_xF_y^-$, $C_xF_y^+$ and $CH_xF^{+/-}$. The top surface also had metallic impurities indicated by Na^+ , $Si^{+/-}$, K^+ , Ca^+ , Mg^+ , Cr^+ , Ni^+ , Fe^+ , $Cu^{+/-}$ and fragments indicative of atmospheric contamination like Cl^- , NO_2^- and NO_3^- . The fragments sputtered from the top niobium oxide layer includes $NbO^{+/-}$, $NbO_2^{+/-}$, NbO_3^- , NbO_4^- , $Nb_2O_2^{+/-}$, $Nb_2O_3^{+/-}$, $Nb_2O_4^{+/-}$ and $Nb_2O_5^-$. The spectrum also included OH^- , $NbOH_x^{+/-}$ from hydroxides or HOH terminating on niobium oxides. It is known fact that secondary ion clusters emanated during SIMS sputtering occurs primarily by atoms that occupy adjacent sites with bonding [33]. It was also realized that smaller fragments like $H^{+/-}$, $C^{+/-}$, $O^{+/-}$ sputtered from various sources that includes, hydrocarbons, amines, oxides, hydroxides, adsorbed water, acidic fragments, reaction products and atmospheric impurities. But, larger fragments were indicators of specific species.

Prior to comparison of the impurities between various treatments, it was necessary to normalize various ion fragments to eliminate errors creeping due to instrumental factors. Nb^+ being an abundant species was used for normalization of all the positive ion fragments. However, the process of normalization applies equal weightage to all the ion fragments, which may not be true. As a result the ratios of each ion fragments with Nb^+ within a treatment was cross checked. Ion fragments of metallic impurities was found to vary independent of Nb^+ counts.

So the results of metallic impurities were decided to be compared using absolute counts. In case of normalization of negative ion fragments the choice was between the total counts or Nb^- . It was found that the results remained similar irrespective of that choice. So, Nb^- was chosen as the normalization factor for negative ions. As we proceed the above choices would obviate into the most probable assumption. After each treatment, the normalized data from three spots of a sample were averaged. Finally, the percentage change of individual species (impurities) of say A^- , between CS polishing and BCP treatment was calculated as

$$\% \text{ Change of } \text{A}^- \text{ after BCP treatment on CS polished samples} = \left[\frac{\left(\frac{\text{A}^-}{\text{Nb}^-} \right)_{\text{BCP}} - \left(\frac{\text{A}^-}{\text{Nb}^-} \right)_{\text{CS}}}{\left(\frac{\text{A}^-}{\text{Nb}^-} \right)_{\text{CS}}} \right] \times 100$$

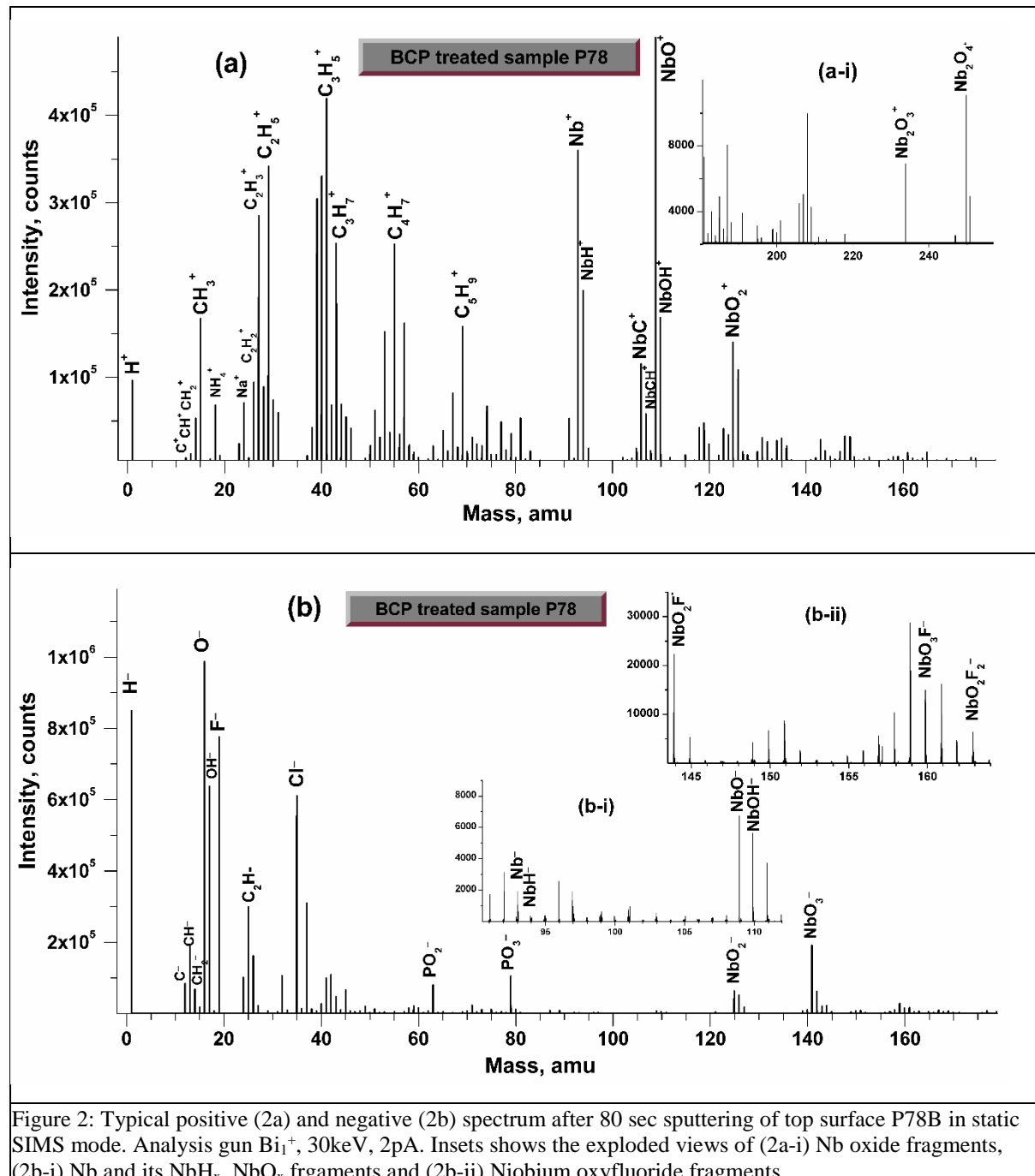


Figure 2: Typical positive (2a) and negative (2b) spectrum after 80 sec sputtering of top surface P78B in static SIMS mode. Analysis gun Bi_1^+ , 30keV, 2pA. Insets shows the exploded views of (2a-i) Nb oxide fragments, (2b-i) Nb and its NbH_x , NbO_x fragments and (2b-ii) Niobium oxyfluoride fragments.

Same procedure was applied for comparing the changes in positive ion fragments. The percentage change of a few negative and positive ion fragments after BCP and HPR treatment on sample P78C and P79C are presented in table 3. It is also well known that repeatability of the performance of SCRF cavities is a matter of concern. So, the spot to spot variation of the ion fragments were also reported after each set of treatment involving P78 and P79 samples. This variation is expressed as percent standard deviation in figure 4. The percent standard deviation (SD) was expressed as

$$\text{Spot to spot variation of } A^- = \left[\frac{\text{Standard Deviation} \left(\frac{A^-}{Nb^-} \right)_{\text{BCP}}}{\text{Average of} \left(\frac{A^-}{Nb^-} \right)_{\text{BCP}}} \right] \times 100$$

Table 3: Table presents the changes in normalized intensities of various positive and negative ion fragments after BCP and HPR treatments on CS polished samples. *Calculation based on Absolute counts.

Normalized negative fragments	Percentage change from CS to BCP		Percentage change from BCP to HPR		Normalized positive fragments	Percentage change from CS to BCP		Percentage change from BCP to HPR	
	P78C to P78B	P79C to P79B	P78B to P78H	P79B to P79H		P78C to P78B	P79C to P79B	P78B to P78H	P79B to P79H
Hydrocarbon fragments in %					Hydrocarbon fragments in %				
H ⁻	-67	-62	18	35	C ₂ H ₃ ⁺	-49	-37	33	38
C ⁻	-48	-42	12	27	C ₂ H ₅ ⁺	-62	-48	33	37
CH ⁻	-59	-53	16	34	C ₃ H ₅ ⁺	-68	-58	49	51
C ₃ H ₂ ⁻	-58	-51	32	40	C ₃ H ₇ ⁺	-83	-76	72	104
C ₃ H ₃ ⁻	-44	-31	39	29	C ₄ H ₇ ⁺	-84	-77	63	87
C ₄ H ₃ ⁻	-75	-71	35	69	NbH ⁺	-45	-44	18	36
NbH ⁻	-65	-62	27	43	CNb ⁺	-16	-22	13	21
CHNb ⁻	-50	-49	30	41	CHNb ⁺	-23	-24	15	15
Niobium oxide fragments in %					Niobium oxide fragments in %				
O ⁻	458	465	-26	-40	NbO ⁺	568	339	-21	-40
OH ⁻	93	106	-3	-14	NbOH ⁺	226	124	-7	-16
NbO ₂ ⁻	1508	843	-20	-40	NbO ₂ ⁺	1,431	884	-37	-59
NbO ₂ H ⁻	268	183	6	-13	Acidic residual/ reaction product fragments in %				
Acidic residual/ reaction product fragments in %					N ⁺	324	255	-34	-32
F ⁻	194194	130087	-87	-87	CH ₂ F ⁺	12,856	14,579	-81	-82
CF ⁻	6542	9429	-80	-82	Metallic impurity fragments in % *				
NO ⁻	676	506	-57	-51	Si ⁺	4	140	54	-17
S ⁻	116	52	239	372	Ca ⁺	-50	166	8852	424
Cl ⁻	3311	4794	-23	-80	Fe ⁺	-84	-60	9083	860
PO ₂ ⁻	8122	21052	-86	-89	Ni ⁺	-22	1029	4923	94
NbO ₂ F ⁻	12608	16336	-91	-93	Cu ⁺	28	79	58,634	37,451
NbO ₂ FH ⁻	2633	4043	-85	-87	Zn ⁺	-85	-74	34,221	12,931

It is clear from table 3, that the hydrocarbons represented by various C_xH_y^{+/} fragments including C⁻, H⁻ reduced by more than 50% after BCP treatment. Moreover, NbH_x^{+/}, NbC_xH_y^{+/} were also found to decrease after BCP treatment. These fragments were also indicative of the hydrocarbon contamination adsorbed on the top of niobium oxide surface. The decrease of hydrocarbon fragments was also confirmed by dramatic increase of NbO_x^{+/} signals.

The $\text{NbO}_x\text{H}_y^{+/-}$ counts were also found to increase parallel to $\text{NbO}_x^{+/-}$ counts. The increase of $\text{NbO}_x\text{H}_y^{+/-}$ counts are indicative of increase in Niobium hydroxides. Presence of niobium hydroxides has been established using XPS technique [34]. Niobium hydroxides formation is related to the water adsorbed on the niobium oxides. It can also form by wet reactions (BCP, CSP, EP) during oxide layer formation. Increase in $\text{NbO}_x\text{H}_y^{+/-}$ counts after BCP also leads to higher OH^- counts. This was further confirmed by the decrease of OH^- counts after HPR treatment which also led to lower $\text{NbO}_x\text{H}_y^{+/-}$ counts. However, OH^- counts does depend on other factors like; amount of water adsorbed on the surface, presence of oxygen and hydrocarbons. The decrease in $\text{NbO}_x\text{H}_y^{+/-}$ counts on the other hand is related to decrease of $\text{NbO}_x^{+/-}$ counts which in turn depends on the hydrocarbon contamination that would be explained later. The large hydrocarbon contamination in P78C and P79C could be related to presence of organic components in the colloidal silica solution itself, whose composition is proprietary. But, between the two sets of treatments the increase of $\text{NbO}_x^{+/-}$ counts was higher in P78 series. The reason was found to be low $\text{NbO}_x^{+/-}$ counts on the P78C samples compared to P79C, whose reason was not clear. Moreover, metallic contaminants like Na^+ , K^+ and Li^+ (not shown here) that were present on P78C and P79C samples, were found to reduce after BCP treatment. Na^+ , K^+ and Li^+ are constituents of the colloidal silica solution used for polishing Nb samples. On the contrary, silicon, which was also a constituent of colloidal silica increased after BCP treatment. The opposite effect could be related to contamination of BCP samples with the Si impurity present in HF acid. However, the actual cause needs to be explored further.

On the other hand HPR treatment was found to re-introduce hydrocarbon and metallic contamination. This unexpected result could either be related to process itself and/or to the extra time ($\sim 1\text{hr}$) that the samples were outside the vacuum chamber in comparison to other samples. Although, HPR processing was carried out in class 100 clean room, still it is an extra step that requires additional time. Consequently the oxide layer was exposed to the atmosphere for longer period. The role of hydrocarbons assumes significance in light of a recent study that proposes link between suppressed superconductivity in Nb and the presence of hydrocarbons near stabilized dislocation bundles [35].

The change in hydrocarbon contamination was also co-related with the OH^-/O^- ratio. This ratio measured using TOF-SIMS has been employed in the past, as an indicator of organic contamination [36]. Higher OH^-/O^- ratio supposedly leads to increased hydrocarbon adsorption and this ratio was found to be independent of SIMS matrix effect [36-37]. The intensity of $^{16}\text{O}^-$ being saturated, we have plotted the average values of OH^-/O^- ratio of each treatment against normalized $\text{C}_x\text{H}_y^{+/-}$, $\text{NbH}_x^{+/-}$, and NbO_x^+ of respective treatments; of which a few are shown in figure 3. The average normalized counts of the ion fragments measured after each treatment, have been scaled up or down to fit the plot. Figure 3, clearly reveals that OH^-/O^- ratio was found to be maximum for colloidal silica polished samples (P78C and P79C) followed by HPR treated samples (P78H and P79H) and finally BCP treated samples (P78B and P79B). Normalized fragments related to hydrocarbons also followed the same pattern. So, OH^-/O^- ratio conclusively establishes the results presented against table 3. Moreover, increasing hydrocarbon contamination leads to simultaneous reduction of the niobium oxide fraction. Additionally, the OH^-/O^- ratio varies linearly with hydrocarbon contamination on the surface. Hence, it can be safely concluded that BCP treatment minimizes hydrocarbon contamination on the top surface of Nb. So, even though the OH^- increase after BCP treatment, it is offset by larger increase of oxygen and $\text{NbO}_x^{+/-}$ counts. Moreover SD percent of hydrocarbons (see figure 4) reveals that the spot to spot variation of hydrocarbon fragments were within $\pm 15\%$, irrespective of treatments.

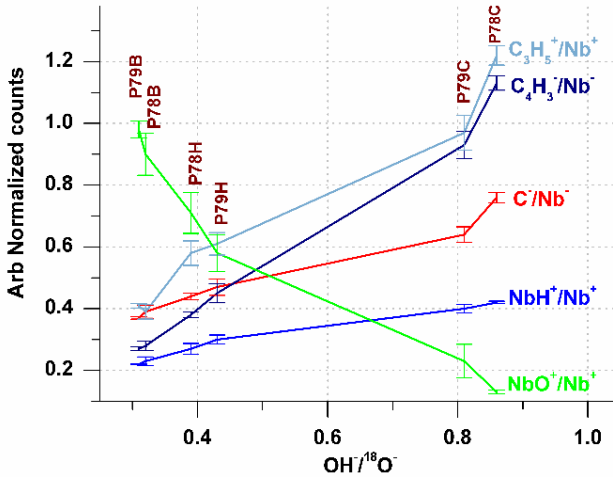


Figure 3: Variation of $\text{OH}^-/^{18}\text{O}^-$ ratio (x-axis) of each treatment plotted against variation of normalized hydrocarbon and oxide fragments (y-axis). The normalized values are scaled up or down to fit the plot.

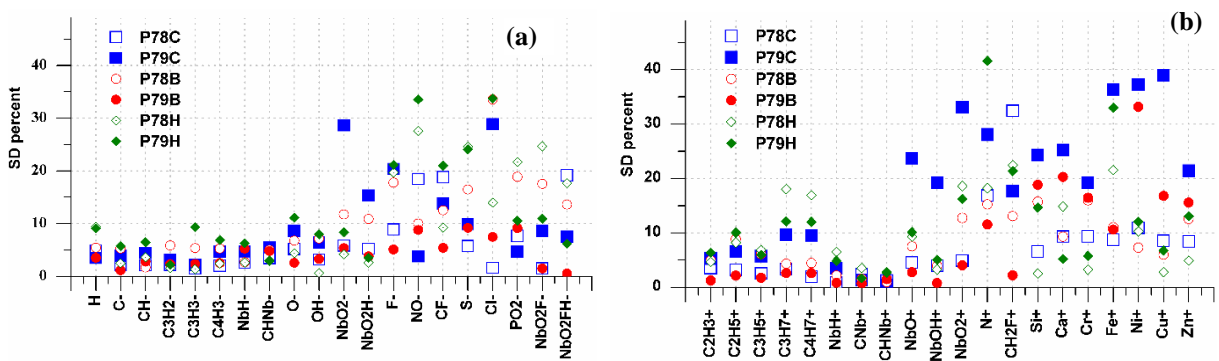


Figure 4: Spot to spot variation of (a) positive and (b) negative fragments at top surface after each treatment for P78C, P79C, P78B, P79B, P78H and P79H. The variation is represented in percentage. (See text for description)

The other major changes after BCP treatment were related to the substantial increase in the intensities of acidic fragments. Table 3 shows that BCP treatment on CS samples led to increase of all acidic fragments by at least 6 times (~500%). F^- intensity was found to increase drastically by more than 1300 -2000 times after BCP treatment. The presence of niobium oxyfluorides fragments, which are reaction products of F^- with niobium pentoxide also increase by 120 times. NbOF^- , NbO_2F^- , NbO_3F^- , NbO_2F_2^- has been used in the past as SIMS signature for fragments sputtered from Niobium oxyfluorides [38]. It would be revealed in section 3.3 that these species contaminate the whole oxide layer of BCP treated samples. HPR treatment on the other hand reduces the acidic contamination on the top layer by dissolution of the acidic residues and niobium oxyfluorides. The reduction is close to 80% of the BCP treated values. Reduction of fluorine by more than 40% has been reported earlier using XPS techniques [39]. HPR treatment also reduces the acidic residues related to phosphoric acid by more than 70%, and nitric acid by 50%. All the above fragments related to acids were found to decrease by at least 50 - 80% after 10 minutes of HPR. The reduction of the acidic contamination after HPR process was similar in both the samples (P78H and P79H). This establishes the effectiveness of the HPR process after any chemical treatment on Nb. Surprisingly, Cl^- also increased dramatically after BCP treatment as it is present as impurities in the acids used. Similar conclusions associated with increase of Cl^- due to HF acid treatment have been proposed earlier

[40]. The reduction of Cl^- counts after HPR treatment, confirms the argument. But it should be noted that Cl^- may also get affected by atmospheric exposure [41]. That was one of the reasons that Cl^- counts were found to increase in few samples that were HPR treated followed by BCP treatment (not in case of P78, P79). The variation of S^- during BCP treatment was not very clear, but as the SD percent graph in figure 4(a) suggests it has very high spot to spot variation. Subsequent increase of S^- after HPR indicates contamination of ultra-pure water by leaching/erosion of sulphur containing compounds from the pipes' walls used for transfer of HPR water. Apart from sulphur, many metallic impurities leached or eroded into the water line.

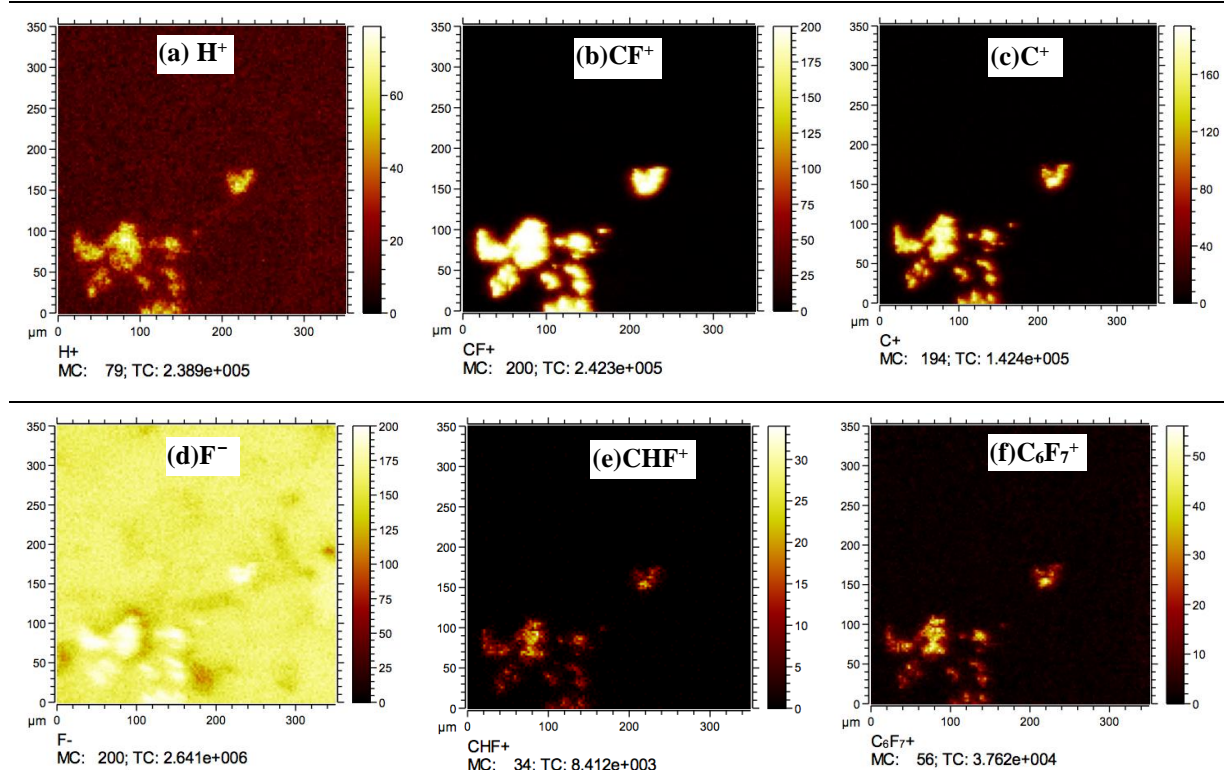


Figure 5: Ion images of BCP treated and marginally rinsed (P89) sample showing enhanced regions of (a) H^+ , (b) CF^+ , (c) C^+ , (d) F^- , (e) CHF^+ and (f) C_6F_7^+ . The bright yellow spots corresponds to maximum intensity of that particular ion; MC = Maximum count, TC= Total counts.

Apart from niobium oxyfluoride, another acidic reaction product was found whose ionic fragments were of the form of C_xF_y^+ , $\text{CH}_x\text{F}^{+/-}$. The origin of this fragment was possibly associated with hydrocarbon products reacting with co-located HF acid residues. The conclusions regarding its origin were based on observations on a different sample (P89) that was BCP treated, but not properly rinsed. The sample was subsequently kept exposed to atmosphere for few days and analyzed in static SIMS mode. The ion images of one such area ($350\mu\text{m} \times 350\mu\text{m}$) exhibited intense localized counts of F^- , H^+ , C^+ , $\text{C}_x\text{F}_y^{+/-}$, $\text{CHF}^{+/-}$ as shown in figure 5. This indicates that improper rinse leads to non-homogeneous distribution of HF residues that can react with hydrocarbons during drying. Presence of such areas with increased C have been reported recently using SEM-EDX [19] and XPS [42] techniques after BCP and EP treatment respectively. But, the results of SEM EDX did not reveal the presence of fluorine, because the signal of fluorine might be insignificant. However, XPS technique, does reveals presence of increased F and C in some areas. Since these fragments were also found to increase in P78B and P79B samples,

so they must be present in all chemically treated surfaces. However, a thorough rinsing minimizes the chances of localized concentration of this contamination. Additionally, the reduction of this fragments after HPR treatment confirms its origin to acidic residuals. This type of contamination can also explain the presence of carbon contamination after BCP treatment that was reported earlier [16]. These fragments also suggests that total counts of H^+ , C^+ is dependent not only on hydrocarbon fragments but also on amount of CH_xF^+ type fragments. The SD percent reveals that the variation of acidic fragments between various spots was significantly high at 25%; which can locally affect the surface properties.

Apart from the impurities associated with colloidal silica solution, Mn^+ and Fe^+ were found to decrease consistently after BCP treatment. Cu^+ on the other hand increased after BCP treatment. The other metallic impurities like Al^+ , Mg^+ , Ca^+ , Ni^+ , Cr^+ did not to follow any specific trend after BCP treatment. However, post HPR, all the metallic contaminants were found to increase dramatically. However, the increase of Si^+ and Cr^+ , counts after HPR was marginal. The source of these metallic contaminations in P78H and P79H was found to be the ultra-pure water used during HPR. But, resistivity of the water measured at the source was $18.2\text{ M}\Omega$, which confirms it as ultra-pure water. This indicates that high pressure water (85kg/cm^2) erodes the surface of stainless steel pipelines, sapphire nozzle and brass connector present in the HPR set up. Hence, erosion was responsible for contamination of UPW by Cr, Ni, Fe, Cu, Zn and Al. Similar results related to increase of Cu and Zn impurities on Nb surfaces, during HPR has been reported earlier [39]. Water analysis of HPR water revealed 5 to 10 times higher Cu (24 - 54 ppb) when compared to the UPW at the source. On the other hand the metallic impurities like Ca, Mg and Si also increased after HPR treatment, which are known impurities of water. However, the source of Ca, Mg and Si impurities was not clear. Since, SIMS is a highly sensitive technique, it was able to detect the changes of metallic impurities that may not have been possible with other techniques.

Figure 3(b) indicates that variation of metallic impurities between different spots is high, irrespective of the type of treatment. It was also observed that apart from spot to spot variability; HPR treated BCP samples had extreme non-homogeneous distribution of metallic as well as non-metallic contamination within a spot (not shown here). Closer inspection of the secondary ion distribution of metallic impurities on sample P78H and P79H along with its corresponding SEM image indicate preferable clustering of metallic impurities near the grain boundary steps, pits and any other steps formed inside grain. Similar results were also obtained during depth profiling of metallic impurities as shown in figure 9(a). This is an important observation as all non-barrel polished cavities have grain boundary steps at the equator region even after electropolishing treatment. Additionally these metallic impurities have magnetic moments that can locally affect the superconducting properties. Moreover, the results on spot to spot variability is well supported by research on FE craters that reveal the presence of variety of metallic and non-metallic species detected using AES and EDX techniques [15].

It is clear from the above discussion that BCP treatment reduces the hydrocarbon fragments thereby increasing the NbO_x^+/Nb^+ ratio in the top layer of Nb, but, leads to extensive contamination by acidic residuals and its reaction products. On the other hand HPR reduces the acidic residuals but re-introduces hydrocarbon contamination along with extensive metallic impurities. However, metallic contamination after HPR treatment can be controlled with improved HPR set up. The results of the static SIMS analysis successfully relates the contamination on the surface to the type of surface treatment. Metallic, non-metallic contaminations that are present on the surface, oxide layer and bulk are primary candidates for diffusion into bulk Nb during subsequent UHV degassing treatment. The

conclusions were based on the depth profile results on sample P115 and P117 that would be presented in section 3.3.

3.2. Oxide depth profile

Figure 6 shows the variation of intensity of various niobium oxide fragments of P78C (CS polished), P78B (CS+BCP treated), P78H (CS+BCP+HPR treated) and P115U (BCP+UHV annealed) samples across the oxide layer. It is known from earlier XPS studies that niobium is covered by a top niobium pentoxide layer followed by sub oxides. To identify various oxides (like Nb_2O_5 , NbO_2 , NbO etc.) using SIMS it is essential to develop SIMS signatures of various oxide fragments plotted after exposing bare Nb surface to pure oxygen and comparing them with niobium oxide crystals of varying stoichiometry. Considering these complications, we limit our discussion to the overall oxide thickness and presence of sub-oxides that seems possible. Earlier SIMS studies has established that if sub-oxides are present then the counts of Nb^+ must be lower than NbO^+ counts near Nb bulk-oxide interface [25, 43]. Another research suggests that intensities of Nb^+ , NbO^+ , and NbO_2^+ peaks should not vary too much before the oxide layer is completely removed [26]. As seen from figure 6, none of the treatments were found to exhibit such pattern. For a clear picture on the thickness, it was necessary to divided into oxide layer in to three zones as shown in figure 6.

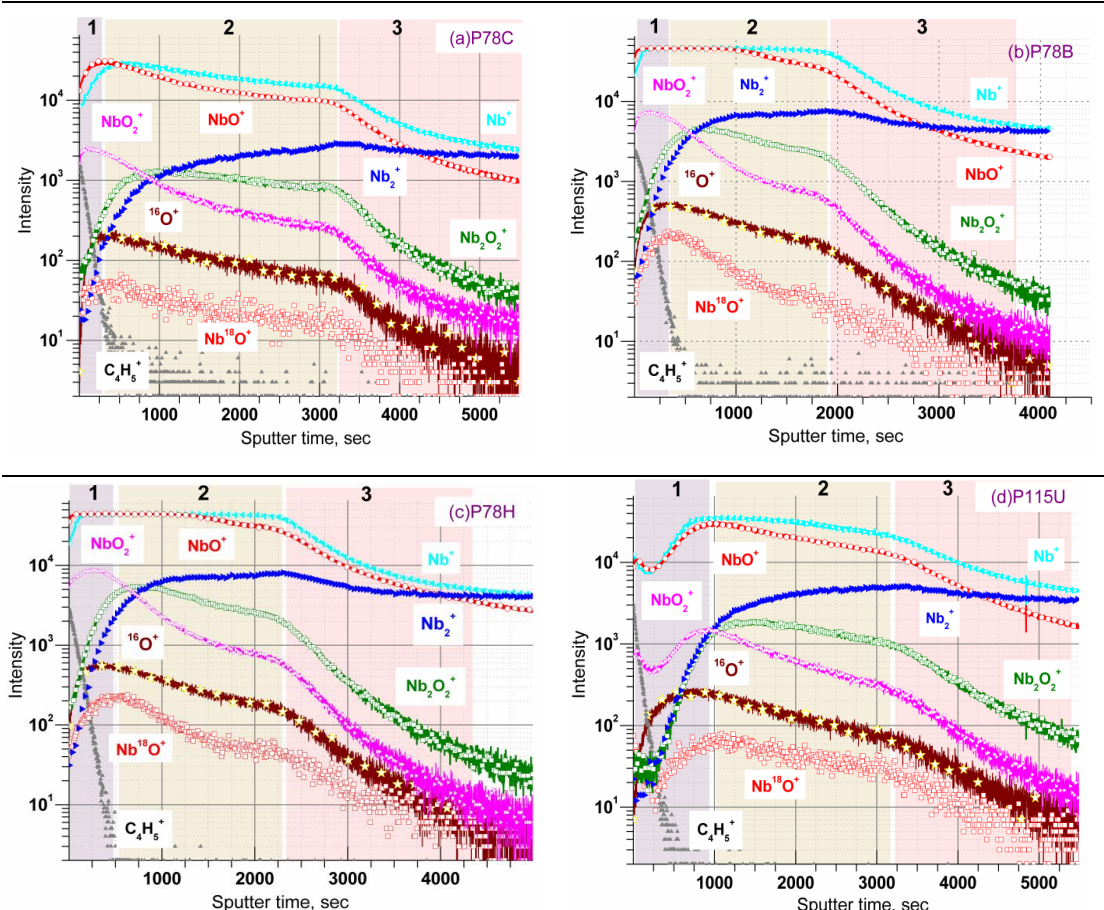


Figure 5: Slow sputtering depth profile of oxide layers of (a) CS polished- P78C, (b) BCP treated- P78B, (c) High pressure rinsed- P78H and (d) UHV degassed at 600°C for 10 hrs- P115U. Analysis done using Bi_1^+ ions at 30kV.

- a) Zone 1- This zone exhibits sharp decline of the hydrocarbon contamination which is represented in the figures by $C_4H_5^+$ counts. The fall of $C_4H_5^+$ counts is almost synonymous with sharp rise of the intensities of various oxide fragments to their maximum values. Hence, the maximum of point $^{18}ONb^+$ was decided as the end of zone 1. $^{18}ONb^+$ was chosen, because NbO^+ counts were saturated in the oxide layer analysis of P78H and P78B. The thickness of the hydrocarbon layer was found to be approximately 1/10th of the total oxide thickness. This is equivalent 0.3 - 0.4 nm thickness which was calculated using data from section 3.3. The values match well with earlier results using XPS techniques [10].
- b) Zone 2- It is manifested by slow decrease in the intensities of various oxide fragments. This zone was considered to extend up to the point where the intensities of oxide fragments started to fall rapidly. The sharp fall also corresponds to the maximum intensities of Nb_2^+ and Nb_3^+ (not shown). This zone may be considered to indicate the pentoxide layer.
- c) Zone 3- The final zone is defined by the end of the oxide layer which results in sharp fall of intensities of oxide fragments along with stabilization of Nb^+ , Nb_2^+ and Nb_3^+ ions. It also coincides with the rise of the NbH_x^+ fragments (not shown here).

These profiles are very similar to what has been observed earlier on buffered electropolished sample [26]. But one major difference exists. The intensity of NbO^+ is higher than Nb^+ in the first 250 – 300 seconds. The reason could be attributed to the difference in the cracking pattern [25] of the hydrocarbon mixed niobium-oxide zone with Bi_1^+ gun as against Au^+ ion used earlier. So, except for the thickness of the second zone and slightly different top zone of P115U, no exceptional difference in the oxide layer was found due to various treatments. This also reflects the similarity of oxide stoichiometry in zone 2 and zone 3, irrespective of surface treatments. Since presence of sub oxides could not be verified we would evaluate the oxide thickness on the basis of the second zone alone. The ratio of the thickness of the second zone between 4 treatments was found to be 1: 1.18: 1.5: 1.9:: P78B: P78H: P115U: P78C (1525: 1800: 2300: 2900). This result indicate that BCP treatment leads to minimum oxide thickness while CS treated samples have double thickness. Similar results would be seen during the depth profile analysis in section 3.3. In other words, the second zone was found to be a good measure of the oxide thickness.

3.3 Depth profile till penetration depth (~50 nm)

The depth profiles were plotted to determine the distribution of various impurities within the Nb penetration depth. The depth profiles obtained using Cs 1keV sputter gun were plotted in figure 7, using the overall average sputter rate of 0.21 nm/sec. The depth profiles compare bulk hydrogen, oxygen, carbon and niobium oxyfluorides contamination among various treatments mentioned in table 2. The depth profile of hydrogen and oxygen are compared using NbH^- and $^{18}O^-$ ion fragments. On the other hand C^- and $NbOF^-$ are also plotted to compare carbon and niobium oxyfluoride contamination. It should be noted that hydrogen contamination produces many fragments like H^- , H_2^- and $Nb_xH_y^-$ (where $x=1-5$, $y=1-4$ with decreasing y as x was increased). Any of these fragments can be used for comparison of hydrogen contamination. In a similar manner NbO^- , NbO_2^- , NbO_3^- can be used for oxygen; NbC^- for carbon and any oxyfluoride fragments mentioned in section 3.1 instead of $NbOF^-$. The results were found to be similar using any ion fragment.

Evaluation of hydrogen contamination has always been critical for SCRF applications. The precipitates of niobium hydride are considered to be most important factor responsible for the undesirable Q-slope and quenching at lower

accelerating fields [7, 44, 45]. Moreover, insitu growth of isolated and large niobium hydride precipitates has been recently observed during cool-down of high purity Nb samples [44], which has been independently confirmed as β -NbH and ϵ -NbH by diffraction patterns using TEM technique [46-47]. Figure 7(a-inset) clearly suggests that NbH contamination in bulk Nb is maximum in CS polishing samples. The contamination in BCP and subsequent HPR treated samples were marginally lower (see inset of 7a). Marginally higher values in CS polished samples may result from higher density of dislocation generated due to the stresses of mechanical polishing. Higher density of dislocation could trap larger quantity of hydrogen. In fact mechanically polished Nb samples had largest hydrides precipitate according to an earlier research [44]. On the other hand, BCP and CS samples that were simultaneously UHV degassed exhibits reduction in bulk hydrogen. But, the surprising observation was, the reduction of NbH^- in sample P117 was only 2.8 times compared to 5.68 times in P115 sample. This difference cannot be generalized in simple terms of H getting trapped under dislocations. Although it is agreed that prior to UHV degassing the density of dislocations in mechanically polished Nb sample (P117C) would be higher than standalone BCP treated sample (P115B). But, the long degassing treatment that involves stress relief, annealing and grain growth would have been sufficient to bring down dislocation density to similar levels in both the UHV degassed samples (P115U, P117U). However, a recent study using Raman spectroscopy has proposed the presence of impurity stabilized dislocation bundles that can trap high levels of C, H, which are resistant to disintegration even during 600°C UHV degassing treatment [35]. In fact, P117C sample has very high concentration of C, metallic impurities and pits compared to samples treated by other techniques. This could explain the difference in hydrogen contamination between P115U and P117U samples. However, the problem needs further investigation in future.

Another interesting feature involving hydrogen evaluation using SIMS technique relates to the presence of intense high resolution peaks of NbH^- , NbH_2^- , NbH_3^- , NbH_4^- , Nb_2H^- , Nb_2H_2^- , Nb_2H_3^- , Nb_3H^- , Nb_3H_2^- , Nb_4H^- , Nb_5H^- in the spectrum obtained from the depth profile in BCP, CS and HPR treated samples. Earlier SIMS studies have also reported existence of niobium hydride fragments upto NbH_4^- [48] and NbH_5^- [7]. This suggests that bulk Nb has unlimited areas to hold hydrogen. Recent ABF and HAADF studies have confirmed presence of β -NbH (face centered orthorhombic structure-FCO) near room temperature after EP and BCP treatment, where H interstitials were shown to occupy tetrahedral site [46]. This has been independently concluded using ERDA technique [8]. This tetrahedral arrangement in fco structure has been considered as 1Nb atom surrounded by 4H atom or vice versa [49]. In fact considering this approach we find that the sputtered fragments of the form Nb_4H^- , NbH_4^- correspond well with the above arrangement of 1Nb atom surrounded by 4H atom or vice versa. Moreover, UHV degassing treatment was found to drastically lower the intensities of the mass fragments containing higher stoichiometric H or Nb than the lower ones. In other words the reduction of NbH^- (lower stoichiometry 1:1) was only 5.68 compared to 44 for NbH_4^- (higher stoichiometry 1:4) when the intensities were compared of UHV degassed sample (P115U) and BCP treated sample (avg P78B, P79B). Please note that the results of depth profiles are similar in P78B, P79B and P115B. The ratio of few other fragments are mentioned in table 4 along with spectrums in figure 8a. The mass spectrum in figure 8a was plotted after cumulative counts acquired from 300 seconds (\sim 60nm) of depth profile of sample P78B and P115U. It should be noted that for comparison purpose, mass spectrum of P78B sample was shifted to the right of P115U. This suggests that UHV annealing is successful in reducing the probability of Nb surrounded by 4H atoms and vice versa, which means that the tetrahedral arrangement of H in Nb is disturbed. This can also be interpreted as reduction of the probability of formation of

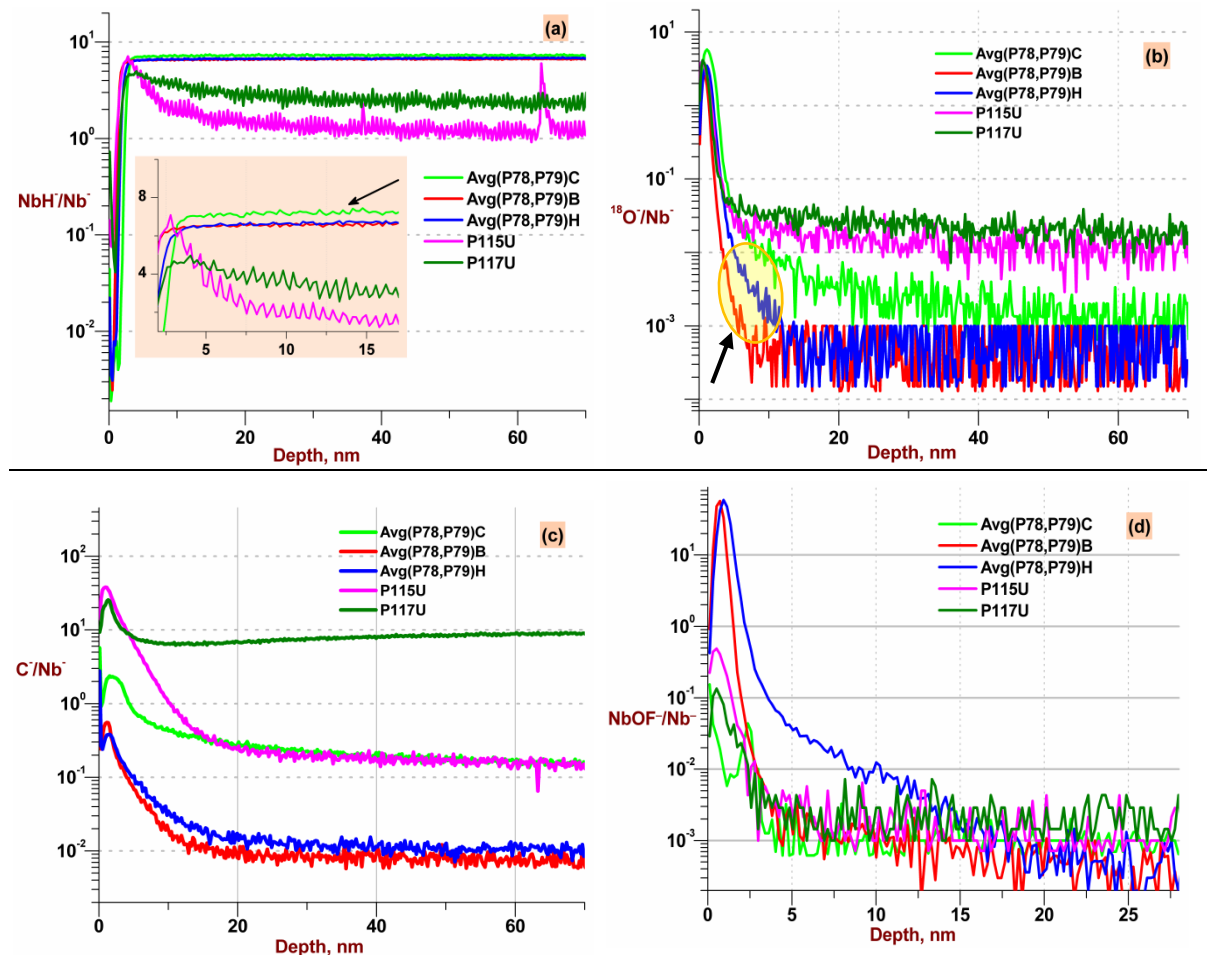


Figure 7: Depth profile of Normalized (a) NbH^- , (b) $^{18}\text{O}^-$, (c) C^- and (d) NbOF^- across the penetration depth of Nb prepared by CS polish, BCP, BCP+HPR, BCP+ UHV, CS+UHV annealing at 600°C for 10hrs. Y axis represents the normalized intensity, while X-axis represents the depth. Inset of figure 7a shows exploded profile of NbH^- near the Nb-oxide bulk interface. The depth profiles are average values of all the spots in all sets of sample.

β -NbH precipitates. In fact absence of NbH precipitates during cool down of UHV degassed Nb samples has been observed by Barkov and his team [44]. It can hence be suggested that the SIMS fragments sputtered using these analysis conditions can serve as an indicator of the arrangement as well as concentration of H within Nb matrix, which in turn relates to the probabilities of hydride precipitation. Further confirmation of this possibility would happen by observing insitu the variations of NbH_x^- fragment ratio during cool down to lower temperatures. The work is in progress and needs re-designing of sample holder.

Table 4: Table 4 measures the normalized NbH_x^- ratio between BCP treated sample and UHV degassed sample. The ratios represent the no. of times the fragments are higher in BCP treated sample.

$\left[\frac{(\text{H}^-)}{(\text{Nb}^-)} \right]_{\text{BCP}}$	$\left[\frac{(\text{NbH}^-)}{(\text{Nb}^-)} \right]_{\text{BCP}}$	$\left[\frac{(\text{NbH}_2^-)}{(\text{Nb}^-)} \right]_{\text{BCP}}$	$\left[\frac{(\text{NbH}_3^-)}{(\text{Nb}^-)} \right]_{\text{BCP}}$	$\left[\frac{(\text{NbH}_4^-)}{(\text{Nb}^-)} \right]_{\text{BCP}}$
3.64	5.68	10.45	17.0	44.12

To eliminate doubts regarding background H playing any role in the depth profiles, an Nb sample with low H intensity or varying H intensity was required. Such NbH^- profile was observed in Nb thin film deposited on Si wafer which was used for sputter rate estimation. Figure 8(a) clearly shows that the NbH^- intensity in Nb thin

film varied by 4 orders from 10^4 counts on surface to zero counts near the Nb-Si interface. Similar hydrogen profile of Nb deposited on wafers has been observed earlier [50].

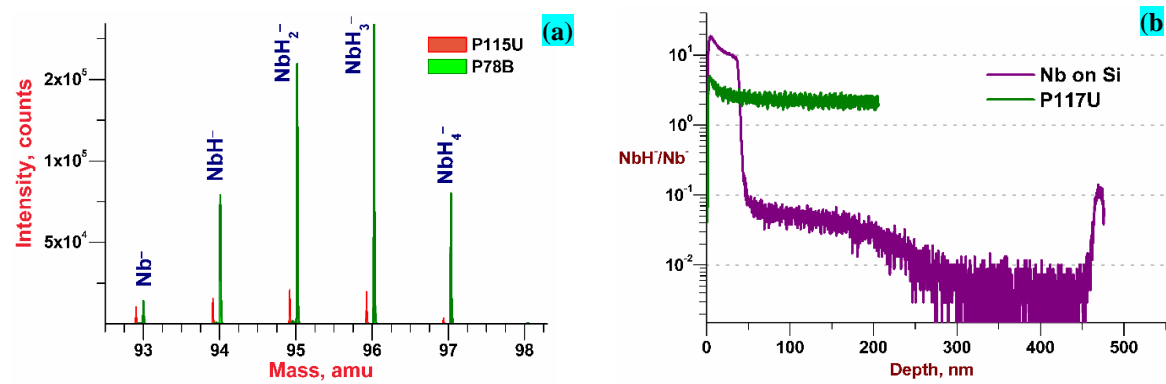


Figure 8: (a) The cumulative mass spectrum of NbH_x^- fragments acquired after 300sec of depth profile of P115U and P78B. The mass spectrum of P78B has been deliberately shifted to the right of P115U for comparison purpose alone (b) The variation of NbH^- in Nb thin film deposited on Si wafer.

The depth profile of oxygen in figure 7(b) clearly distinguish the top oxide layer by sharp rise and fall of $^{18}\text{O}^-$ intensity. Once the oxide layer is removed a stable Nb^- signal was observed. The depth at which the Nb^- signal reaches a constant value was used to determine the interface between the surface oxide film and the bulk niobium. Based on this, the oxide thickness was estimated to be 2.77 ± 0.09 nm for BCP treated sample, 3.71 ± 0.6 nm for HPR sample and 4.34 ± 0.38 nm for CS samples. The thickness of UHV sample could not be estimated correctly using the above method, because Nb intensity stabilized after ~ 15 nm depth. This could be related to the higher and varying oxygen content within UHV degassed samples. However considering partial stabilization of Nb^- counts, the thickness was estimated to be 3.8 nm. The thickness observed are on the lower side of the values reported in the literature which ranges from 2 - 6 nm [10, 12, 26, 51, 52]. But, lower values are possible since the samples were loaded within 30 minutes of the final preparation step (except for P115U and P117U). Earlier studies using TEM techniques have also reported oxide thickness of ~ 3 nm after BCP treatment [53]. In fact our BCP treated samples that were analyzed after exposure to atmosphere for 2 days had an oxide thickness of 3.82 ± 0.1 nm. Hence, within the experimental conditions, BCP treated Nb has minimum oxide thickness while CS samples have maximum thickness. Marginal increase in oxide thickness after HPR has been observed, to which we would come back later. In contradiction to earlier results stating non-uniformity of oxide thickness on Nb samples [26, 54], our BCP treated samples were extremely uniform. Moreover, the ratio of the oxide thickness after 4 different treatment matches is 1: 1.33:1.37: 1.56:: P78B: P78H: P115U: P78C. The trend of the ratio matches well with results obtained in section 3.2. Marginal variation of the ratio could be related to the presence of impurity deposits on the surface of HPR, UHV and CS polished samples. On the other hand, oxygen content was found to be 10 times higher in bulk Nb of annealed sample (P115U, P117U) and 5 times higher in CS treated samples (P78C, P79C) compared to BCP treated sample. The increase of 10 times is higher than ~ 6 times observed earlier [7]. However, the increased oxygen content in P115U and P117U indicates dissolution of oxygen into the bulk during annealing, inspite of very good vacuum. But, higher oxygen content in CS polished samples was related to the presence of Si impurities inside the bulk niobium. These Si impurities were found to be surrounded by oxygen as revealed by the ion images (not shown here). The elevated oxygen levels in the bulk Nb may be detrimental to

superconducting properties as high oxygen content reduces T_c [22] and increases surface resistance [21]. The oxygen depth profile also indicated increased oxygen intensity at the interface between the oxide and bulk Nb, for HP rinsed BCP samples. The increased oxygen intensity at the interface is shown encircled in figure 7b. Since HPR is related to surface cleaning it is impossible to change the interface oxygen content. However, a closer inspection revealed that increase of oxygen at interface after HPR treatment was a SIMS artifact. The artifact can be explained on the basis of metallic impurity deposits that was observed on HPR treated samples (P78H and P79H). It has been already revealed in section 3.1 that HPR treated BCP samples had very high metallic impurity contamination on their surfaces forming clusters near grain boundary step, pits, sub steps inside grains and any location that had difference in heights. Similar results were observed during depth profiling. Fig 9 shows the ion image of such an area along with its corresponding SEM image. Figure 9a-9b shows the cumulative ion image (the total depth) of Cu^- and O^- , while figure 9d-9e shows the cross-section image (across the depth) of the same location. Figure 9f shows the ion image overlay of Cu^- (pink) and O^- (blue) shown. It clearly shows copper impurities present over the oxide surface. Same observations were made for all other metallic impurities.

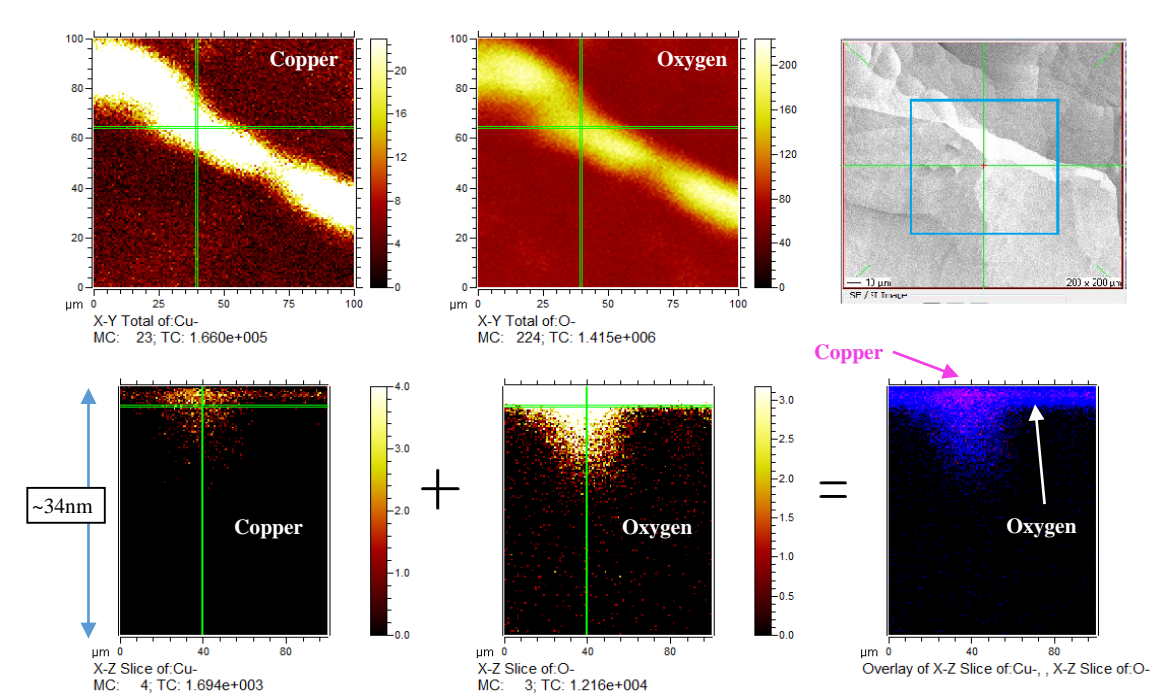


Figure 9: Secondary ion images of $100 \times 100 \mu\text{m}^2$ area with a resolution of 128×128 pixels of (a) Cu^- , (b) O^- , (c) The secondary electron image of the same spot in a $200 \times 200 \mu\text{m}^2$ area, (d) XZ slice of Cu along the horizontal green line, (e) XZ slice of O^- along the horizontal green line (f) Red and blue overlay of Cu^- and O^- respectively near a grain boundary step in P79H sample after HPR. (9c). The counts of individual ion fragments in each pixel are shown in the intensity scale on the right of images. The bright yellow spots corresponds to maximum intensity of that particular ion; MC = Maximum count, TC = Total counts. The ion images were slightly conditioned using TOFSIMS software for the purpose of proper viewing without affecting the originality.

Using this background, the exploded profile of the area was sketched in figure 10(a). Figure 10(a) depicts the pristine surface of high pressure rinsed BCP treated sample. Orange colored deposit resembles copper metallic deposit as an example. It is clear from figure 10(a), that, when the Bi_1^+ gun analyses oxygen from oxide layers at portions 'a' and 'b', the oxygen at portion 'c' remains embedded under the Cu or any other metallic deposit. So

the oxygen at portion 'c' would show up in the depth profile when the oxide layer ($\sim 3\text{nm}$) is partially or completely removed at location 'a' and 'b' by the sputter gun as shown in figure 10(b). So even though $\sim 3\text{ nm}$ is removed, oxygen remains on the surface due to the location 'c'. This remaining oxygen, shows up as marginally higher intensity near the interface. This creates an illusion in the depth profile of HPR samples as seen in figure 7(b). This assumption was further confirmed when impurities that are trapped inside oxide layer (like C^- , F^- , P^- , PO_x^- , NbO_xF_y^- etc.) also exhibited similar depth profiles (see figure 7c, 7d for C^- and NbOF^- respectively). Moreover, such SIMS artifact was found missing in areas analyzed without grain boundary steps, pits and substeps. Infact, the metallic deposits (Cu, in this case) itself show their presence inside Nb sample, which in reality is present on the surface only. In other words, greater is the thickness of the metallic deposit on the surface of Nb, deeper would be its presence shown during the depth profile of the metallic impurity. Based on this argument; it can be concluded that the height of these metallic deposits would be closely equivalent to the extended depth to which it shows in the depth profile in comparison to the BCP treated samples. The calculation of the heights would be done later as shown in figure 11. However, presence of metallic impurities inside flat grains could neither be denied nor confirmed. But, earlier research have indicated that the oxide thickness increases with increasing water dose during HPR [55]. Surprisingly they have earlier reported the presence of higher Cu, Zn on their HPR treated Nb surface [39]. So, the increased oxide thickness after HPR treatment is a matter of conjecture and requires further studies. Moreover, this type of artefact may go undetected in most of the surface analytical techniques. In fact the observations by early researcher indicating non-uniformity of oxide thickness [54] can also be explained on this basis of impurities on the top surface of Nb.

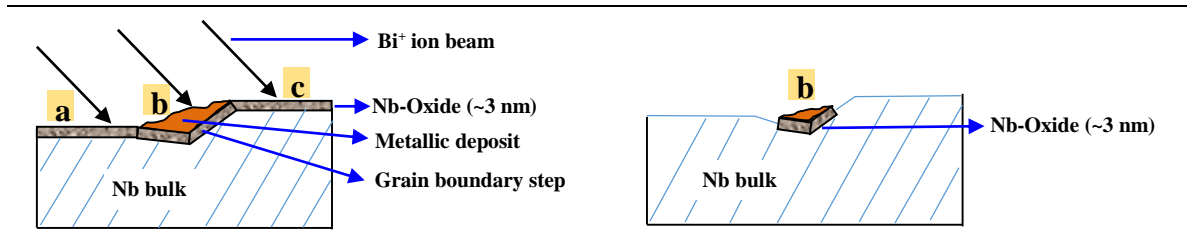


Figure 10: Sketch to represent the metallic deposits found on P78H, P79H as seen from ion images in figure 9. (Left) Pristine Nb surface after HPR treatment; (Right) After oxide layer is removed by sputter gun.

The variation of carbon, within the penetration depth of Nb, was compared among various treatments as shown in figure 7(c). Carbon impurities were found to be highest in CS polished and UHV degassed samples. High carbon in CS treated sample (P78C, P79C) was due to SiC particles embedded inside Nb, during rough polishing steps. This was confirmed by high and stable intensity of Si, which were present in some spots, till $3\mu\text{m}$ depth. Additionally, carbon intensity inside penetration depth is at least than 10 times higher in UHV annealed samples than BCP treated and HPR treated samples. Hence, higher intensity of carbon in UHV annealed samples seems to be related to the initial carbon concentration at the surface and the contamination in the furnace chamber. The depth up to which the carbon diffused in P115U was close to 800- 900nm. The role of initial carbon was confirmed by comparing the C profile in P117U (CS polished and UHV degassed) and P115BU (BCP treated and UHV degassed) samples that were loaded in the furnace simultaneously. The intensity of carbon in bulk Nb of P117U sample was 2 orders higher than P115U which was similar to the ratio of carbon intensity in CS (P78C, P79C)

and BCP treated (P78B, P79B) samples. This confirms that the previous treatment has a role in deciding the impurity distribution inside bulk Nb after subsequent treatments. There is a high probability that the extra carbon that is present in UHV degassed samples would tend to transform into niobium carbide, owing to its limited solid solubility in Nb [56]. The other possibility of existence of carbon could be near dislocations bundles as suggested earlier [35].

The counts of nitrogen in depth profile mode, were too less to extract any meaningful conclusion. Although $\text{NbN}^{+/-}$ fragment has been used by researchers [7] for comparison, but this method has a major drawback of mass interference with $\text{NbCH}_2^{+/-}$ fragment which should not be overlooked.

Figure 7d clearly indicates intense accumulation of niobium oxyfluorides inside the oxide layer of Nb after BCP treatment. Other oxyfluoride fragments that were found in BCP treated sample include NbF^- , NbOF^- , NbOFH^- , NbO_2F^- , NbO_2FH^- , NbO_3F^- and NbO_2F_2^- which are known to be SIMS fragments sputtering out from niobium oxyfluorides [38]. The oxide layer was also found to be loaded with PO_x^- , NO^- , and F^- . Although presence of PO_x^- after BCP has been reported, we could not find such mention regarding niobium oxyfluorides. F and P impurities were found to increase by 2 orders at the Nb surface after BCP treatment. This increase was confined to the top 2 nm depth for P. But, fluorine was found to diffuse inside bulk Nb. The depth up to which fluorine was found in BCP treated and HPR rinsed BCP samples was close to 700 –800 nm (not shown here) in contrast to 150 nm that has been reported earlier [15]. HPR treatment was successful in reducing the acidic contamination on the top surface of Nb. However, the contamination of the oxide layer and bulk of HPR sample remained similar to BCP treated samples. High intensity at the interface, after HPR treatment is an artifact whose reason has been already explained. UHV annealing reduces the F content drastically to levels observed in CS polished samples.

Depth profile of metallic impurities were measured using O_2^+ ion gun at 500 eV as sputter gun. Since, proper normalization factors were not found, so absolute values are compared. The result presented here are limited to comparison only and are not absolute concentration. Figure 11 compares the changes in Fe and Cu resulting due to various treatments listed table 2. Other metallic impurities were found to follow the above pattern. Four distinguishable features that are visible from the depth profiles of Fe and Cu in figure 11 are listed.

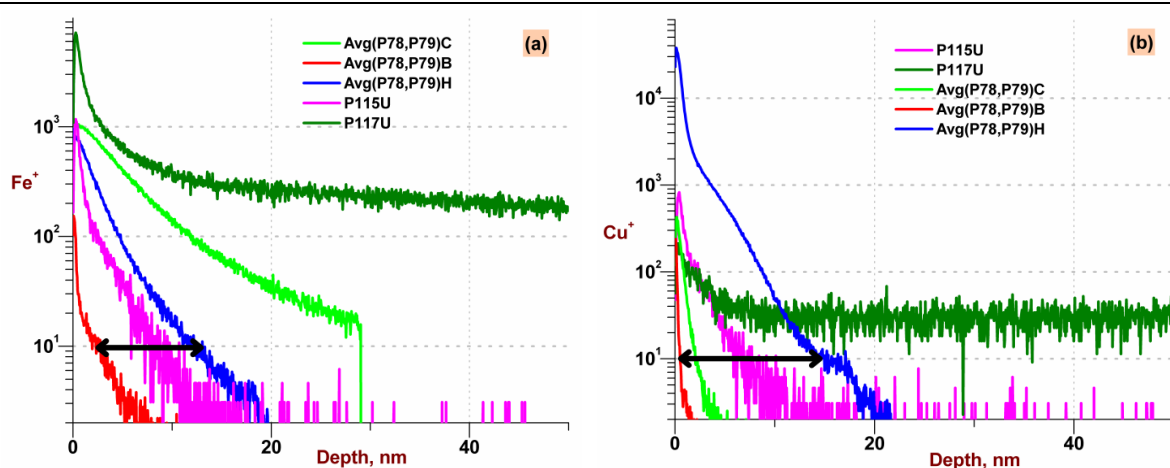


Figure 11: Depth profiles of metallic impurities of Fe and Cu after the various treatments listed in table 2.

- i. Fe and Cu contamination in P117U sample was found to be higher than CS polished samples and were present with increased intensity, throughout the penetration depth.
- ii. In a manner similar to point (i), Fe and Cu contamination in P115U sample was higher than BCP treated samples, but lower than P117U sample. The ratio of increase of Fe and Cu between BCP treated samples and P115U was almost similar to CS treated and P117U sample. Similar results were observed for Si, Na, Mg, Al, Ca, Cr and Ni. The depth profile of carbon shown earlier also indicated a similar trend. This indicates that impurities existing on the Nb surface prior to UHV degassing treatment has a role to play. Another source of impurities in bulk Nb could be related to the contaminations present in the furnace itself. Reports in literature have indicated rise of residual resistance in SCRF cavity after 600°C UHV annealing [7, 17]. This was evident from the increase in the metallic, carbon and oxygen impurities after UHV annealing treatment. Additionally, thermometry studies on UHV degassed cavities had suggested that the hot spots were observed at areas where it existed prior to the UHV degassing treatment. This is evident from the much higher contamination of carbon and metallic impurities including Si in P117 sample compared to P115 sample.
- iii. BCP treatment was successful in reducing the Fe and Cu metallic contamination acquired during CS polishing. Infact the contamination was lowest in BCP treated samples among all treatments. In line with this observation, metallic impurities in CS polished samples were found to have very high intensity near the top surface, followed by constantly decreasing values with depth. Metallic contamination like Li, Na, Mg, Al, K, Ca, Mn, Ni and Fe were almost 4 - 10 times higher within the first 5–10nm compared to BCP treated samples. Thereafter, the intensity of these impurities kept decreasing within bulk Nb and was found extending to a depth of 10 - 20 nm for Li, Mn and Ni; 30–40nm for Na, Mg, Al, Ca and Fe. Si contamination in CS polished samples were found to be much higher as explained earlier. The diameter of these particles varied from 8-14 μ m. On the other hand impurities like Cr, Zn were almost similar in CS and BCP treated samples. These results are based on the maximum detection limits of the TOFSIMS instrument.
- iv. Fe and Cu contamination in HPR treated BCP samples show very high intensity at the surface and fount to be present to an extended depth in comparison to BCP treated samples. Higher intensity of metallic impurities at the surface of HPR treated samples co-relate well with our results presented in section 3.1. However, presence of these metallic impurities to an extended depth is a SIMS artifact, which has been explained earlier. Similar results were observed for Ca^+ , Ni^+ , Cr^+ , Cu^+ and Zn^+ . Using the analogy presented earlier, the heights of the metallic deposits were calculated. The difference between the actual depth of impurity and the artifact in HPR treated samples are represented by the arrow shown in figure 11. The heights of the deposits were 3-4 nm for Al, Cr and Mn; 10 - 15nm for Fe, Ni, Cu and Zn. These values co-relate well with the extended depth of $^{18}\text{O}^-$ and NbOF^- of HPR samples shown figure 9b and 9d respectively. The values are approximate, since the sputter rates of these deposit would be different from sputter rates calculated above. It is clear from the above results that erosion of metallic surfaces which comes in the path of high pressure water is responsible for contamination of the HPR water, which in turn contaminates the Nb surfaces.

Hence, it can be concluded that BCP treatment results in minimum metallic contamination. On the other hand the advantage of reduction of hydrogen contamination during UHV annealing was offset by the presence of increased

metallic impurities. It should also be emphasized that metallic impurities were non-homogeneously distributed in all samples except BCP treated samples. However, none of the UHV degassed samples exhibited segregation of metallic/ no-metallic impurities along the grain boundaries. However, our recent analysis of Nb samples degassed above 1000°C does exhibit segregation of few metallic impurities near grain boundaries. This result would be dealt in our future studies.

4. Conclusions

TOF-SIMS technique was extensively and successfully applied to compare the vast spectrum of impurities in high purity Nb samples after various treatment simulating SCRF cavity processing. The manuscript has used a step wise impurity analysis procedure that includes; impurity distribution on top monolayer of Nb surface using Static SIMS technique; the oxide layer investigation by slow sputtering technique and impurity distribution within the penetration depth (~50nm) by dual beam dynamic TOF-SIMS technique. The results clearly indicate that hydrogen impurity levels inside the bulk Nb was highest in CS polished samples. BCP treated and subsequently HPR samples had marginally lower H contamination than CS polished samples. But, the large reduction in H contamination was possible by UHV degassing treatment at 600°C for 10 hrs. It was also successful in drastic reduction of larger NbH_x ion fragments like NbH₄⁻, Nb₄H⁻. It was also observed that impurities found inside Nb after UHV degassing treatment were related to the impurities left over by previous treatments. For example, carbon levels in BCP treated UHV degassed sample were much lower than the sample that was UHV degassed after CS polishing. Hence, the advantage of reduction of H during UHV annealing was offset by the presence of increased carbon, oxygen and metallic impurities. BCP treatment, on the other hand, was capable of reducing the hydrocarbon contamination of the Nb surface along with metallic contamination in the bulk Nb acquired during CS polishing treatment. However, BCP treatment led to extensive contamination of the oxide layer by acidic residuals and acidic reaction products. Fluorine contamination was found to increase by 2 orders in BCP treated sample in comparison to CS polished samples and extended beyond the penetration depth (800 - 900nm). HPR treatment on the other hand was successful in reducing the acidic contamination on the surface of niobium, but led to non-homogeneous distribution of metallic and non-metallic impurities of Nb surface. The oxide layer was found to be uniform and thinnest at ~2.7nm after BCP treatment. However, the thickness of oxide layers of CS polished and HPR treated samples were not only non-uniform, but also thicker than BCP treated samples. Presence of sub-oxides could not be confirmed after any of the treatments, using slow depth profile technique. Moreover, the oxide stoichiometry was found to be similar, irrespective of the type of treatments. Except for BCP treated samples, all other treatment led to non-homogeneous distribution of metallic impurities within an analysis spot. This study clearly indicates that various impurities within the penetration depth of niobium are very sensitive to the type of treatment and its sequence. The next step of this study would use the current set of results to analyze the complex EP treatment followed by low temperature baking. Further study is also needed for quantification of various impurities.

Acknowledgement

Authors are thankful to Dr. P. D. Gupta, Director, Raja Ramanna Centre for Advanced Technology for the encouragement received for publishing this work. We wish to thank Dr. P. Ramsankar and Shri B. Q. Khattak,

CTF, RRCAT for helping in water analysis. We also express our sincere thanks to Dr. C. Mukherjee and his team for preparing the Nb thin film specimen.

5. References

1. Joshi S C, Roy S B, Hannurkar P R, Kush P, Puntambekar A, Shrivastava P, Mundra G, Dwivedi J, Khare P and Gupta P D 2012 R&D activities on high intensity superconducting proton linac at RRCAT *Proceedings of LINAC2012 (Tel-Aviv, Israel)*, 843-845
2. Jana A R, Kumar V, Kumar A and Gaur R 2013 Electromagnetic Design of a $\beta_g = 0.9$, 650 MHz Superconducting Radiofrequency Cavity *IEEE Transactions on Applied Superconductivity* **23**(4) 3500816
3. Wiener J and Padamsee H 2008 High Field Q-Slope Onset in EP and BCP Cavities Before Bake *SRF reports* 080326-06 1-3
4. Lilje L et al 2004 Improved surface treatment of the superconducting TESLA cavities *Nuclear Instruments and Methods in Physics Research A* **516** 213-227
5. Visentin B, Charrier J-P, Aspart A, Gasser Y, Poupeau J-P and Congretel G 2002 A non-electropolished Niobium cavity reached 40 MV/m at Saclay *Proceedings of EPAC2002 (Paris, France)* 2292-94
6. Lengeler H 1978 RF superconductivity:expectations and achievements *Cryogenics* **18** 8 465-471
7. Ciovati G, Myneni G, Stevie F, Maheshwari P and Griffis D 2010 High field Q slope and the baking effect: Review of recent experimental results and new data on Nb heat treatments *Phys. Rev. Spec. Top. Accel. Beams* **13** 022002 1-20
8. Romanenko A and Goncharova L V 2011 Elastic recoil detection studies of near-surface hydrogen in cavity-grade niobium, *Supercond. Sci. Technol.* **24** 105017
9. Aspart A, Eozénou F and Antoine C 2006 Aluminum and sulfur impurities in electropolishing baths, *Physica C* **441** 249-253
10. Ma Qing and Rosenberg R A 2003 Angle resolved XPS study of the oxides of Nb surfaces for superconducting r.f. cavity applications *Appl. Surf. Sci.* **206** 209-217
11. Ciovati G 2006 Improved oxygen diffusion model to explain the effect of low-temperature baking on high field losses in niobium superconducting cavities *Appl. Phys. Lett.* **89** 022507 1-3
12. Delheusy M, Stierle A, Kasper N, Kurta R P, Vlad A, Dosch H, Antoine C, Resta A, Lundgren E and Andersen J 2008 X-ray investigation of subsurface interstitial oxygen at Nb/oxide interfaces *Appl. Phys. Letters* **92** 101911 1-3
13. Casalbuoni S, Knabbe E A, Kotzler J, Lilje L, Sawilski L V, Schmuser P and Steffen B 2005 Surface Superconductivity in Niobium for Superconducting RF Cavities *Nucl. Instrum. and Methods in Phys. Res. A* **538** 45-64
14. Padamsee H 2009 RF superconductivity Science, Technology and Applications (Weinheim: Wiley–VCH) 65, 87, 93, 96, 171
15. Hays T, Klauda M, Knobloch J, Moffat D, and Padamsee H 1993 Microscopic Examination and Elemental Analysis of Field Emission Sites in 5.8 GHz Superconducting Mushroom Cavities *Proceedings of the Sixth Workshop on RF Superconductivity (Virginia, USA)* 750-762
16. Dacca A, Gemme G, Mattera L and Parodi R 1998 XPS analysis of the surface composition of niobium for superconducting RF cavities *Applied Surface Science* **126** 219–230
17. Antoine C, Bonin B, Safa H, Berthier B, Tessier C, Tocellier P, Chevarier A, Chevarier N, and Roux B 1997 Evidence of preferential diffusion of impurities along grain boundaries in very pure niobium used for radio frequency cavities, *Journal of Applied physics* **81** 1677-1682
18. Tyagi P V 2010 Surface analyses of electropolished niobium samples for superconducting radio frequency cavity *J. Vac. Sci. Technol. A* **28** (4) 634-638
19. Kato S, Hayano H, Kubo T, Noguchi T, Saeki T and Sawabe M 2013 Study on niobium scratch and tantalum or carbonaceous contaminant at niobium surface with field emission scanner, *Proceedings of SRF2013 (Paris, France)* 731-735
20. Ozelis J 2011 Observations of Spontaneous Field Emission Occurrence with Subsequent Cavity Performance Degradation *TTC Meeting 28 February – 2 March, 2011 Milan*

21. DeSorbo W 1963 Effect of Dissolved Gases on Some Superconducting Properties of Niobium *Phys. Rev.* **132**(1) 107-123
22. Abrikosov A A and Gorkov L P 1961 Contribution to the theory of superconducting alloys with paramagnetic impurities *Sov. Phys. JETP* **12** 1243-53
23. Muller A and Benninghoven A 1973 Investigation of surface reactions by the static method of secondary ion mass spectrometry, III. The oxidation of vanadium, niobium and tantalum in the monolayer range *Surface Science* **39** 427-436
24. Dawson P H and Tam W C 1979 The interaction of oxygen with polycrystalline Nb studied using AES and Low energy SIMS *Surface Science* **81** 464-478
25. Wu A T 2006 Investigation of oxide layer structure on niobium surface using a secondary ion mass spectrometry *Physica C* **441** 79-82
26. Wu A T, Mammoser J, Phillips L, Delayen J, Reece C, Wilkerson A, Smith D and Ike R 2007 Smooth Nb surfaces fabricated by buffered electropolishing *Applied Surface Science* **253** 3041-3052
27. Ciovati G, Kneisel P and Gurevich A 2007 Measurement of the high-field Q drop in a high-purity large-grain niobium cavity for different oxidation processes *Physical review special topics – Accelerators and beams* **10** 062002 1-19
28. Tian H, Reece C E, Kelley M J, Wang S, Plucinski L, Smith K E and Nowell M M 2006 Surface studies of niobium chemically polished under conditions for superconducting radio frequency (SRF) cavity production *Applied Surface Science* **253** 1236-1242
29. Hahn H and Halama H J 1976 AES depth profile measurements of niobium for superconducting cavities *Journal of Applied Physics* **47**(10) 4629-4634
30. Marhauser F, Kneisel P, Burrill A, Kushnick P, and Rimmer R A 2011 Preliminary test results from 650 MHz single cell medium beta cavities for project X *Proceedings of SRF2011 (Chicago, USA)* 271- 274
31. Roth R 1993 Untersuchungen zu anomalen Verlusten in Niobresonatoren *Ph.D. Thesis Universität Wuppertal WUP-DIS 92-12*
32. Wu A T, Jin S, Lu X Y, Rimmer R A, and Zhao K 2011 Effects of the thickness of Niobium surface oxide layers on field emission *Proceedings of IPAC2011 (San Sebastián, Spain)* 355-357
33. Benninghoven A and Muller A 1973 Investigation of surface reactions by static method secondary ion mass spectrometry II. The oxidation of Chromium in the monolayer range, *Surface Science* **39** 416-426
34. Grundner M and Halbritter J 1984 On the natural Nb₂O₅ growth on Nb at room temperature *Surface Science* **136** 144-154
35. Cao C, Ford D, Bishnoi S, Proslier T, Albee B, Hommerding E, Korczakowski A, Cooley L, Ciovati G, and Zasadzinski J F 2013 Detection of surface carbon and hydrocarbons in hot spot regions of niobium SRF cavities by Raman spectroscopy *Phys. Rev. ST Accel. Beams* **16**, 064701 1-9
36. Takeda S, Fukawa M, Hayashi Y and Matsumoto K 1999 Surface OH group governing adsorption properties of metal oxide films *Thin Solid Films* **339** 220-224
37. Takeda S and Fukawa M 2005 Role of surface OH groups in surface chemical properties of metal oxide films *Mat Sci and Engg. B* **119** 265-267
38. Singh S, Festin M, Barden W R T, Xi L, Francis J T, and Kruse P 2008 Universal Method for the Fabrication of Detachable Ultrathin Films of Several Transition Metal Oxides *ACS Nano* **2**(11) 2363-2373
39. Tyagi P V, Hayano H, Nishiwaki M, Sawabe M, Kato S and Saeki T 2010 Various rinsing effects to mitigate contaminants brought by BCP on Nb SRF cavity surface *Proceedings of IPAC 10 (Kyoto, Japan)* 2968-2970
40. Kempson I M, Barnes T J, and Prestidge C A 2010 Use of TOF-SIMS to Study Adsorption and Loading Behavior of Methylene Blue and Papain in a Nano-Porous Silicon Layer *Journal American Soc Mass Spectrom* **21** 254-260
41. Hashimoto M, Watanabe E, Amano C, Haraki T, Nishi Y and Uchida H-H 2008 Analysis on nitrogen oxides by TOF-SIMS *Applied Surface Science* **255** 1544-1546
42. Nishiwaki M, Hayano H, Kato S, Saeki T, Sawabe M and Tyagi P V 2010 Surface study on Niobium stain after electropolishing for super-conducting RF cavity *Proceedings of IPAC10 (Kyoto, Japan)* 2941-2943
43. Plog C, Wiedmann L and Benninghoven A 1977 Empirical formula for the calculation of secondary ion yields from oxidized metal surface and metal oxides *Surface Science* **67** 565-580

44. Barkov F, Romanenko A, and Grassellino A 2012 Direct observation of hydrides formation in cavity-grade niobium *Physical rev Spec Topics-Accel and beams* **15** 122001 1-6
45. Isagawa S 1980 Hydrogen absorption and its effect on low temperature electric properties of niobium *Journal of Applied Physics* **51** 4460-4470
46. Kim Y-J, Tao R, Klie R F and Seidman N 2013 Direct Atomic-Scale Imaging of Hydrogen and Oxygen Interstitials in Pure Niobium Using Atom-Probe Tomography and Aberration-Corrected Scanning Transmission Electron Microscopy *ACS Nano* **7**(1) 732–739
47. Trenikhina Y, Zasadzinski J and Romanenko A 2013 Nanostuctural TEM/STEM studies of hot and cold spots in SRF cavities *Proceedings of SRF2013 (Paris, France)* 504-507
48. Zuchner H, Bruning T 1995 SIMS investigations on the system NbH_n(D_n) (0<n < 1) *Journal of Alloys and Compounds* **231** 347-353
49. Garces J 2014 Short-range order of H in the Nb-H solid solution *International journal of hydrogen energy* **39** 8852-8860
50. Valderrama E F, James C, Krishnan M, Zhao X, Phillips L, Reece C and Seo K 2012 High-RRR thin-films of NB produced using energetic condensation from a coaxial, rotating vacuum ARC plasma (CEDTM) *AIP Conf. Proc.* **1434** 953-960
51. Nishiwaki M, Hayano H, Kato S, Saeki T, Sawabe M and Tyagi P V 2009 Surface study using Niobium sample coupons for superconducting RF cavity *Proceedings of PAC09 (Vancouver, Canada)* 984-986
52. Grundner M and Halbritter J 1980 XPS and AES studies on oxide growth and oxide coatings on niobium *Journal of Applied Physics* **51**(1) 397-405
53. Wu A T, Gu D and Baumgart H 2009 TEM study of Niobium surfaces treated by different polishing techniques *Proceeding of SRF 2009 (Berlin, Germany)* 300-304
54. Halbritter J and Darlinski A 1987 Angle resolved XPS studies of oxides at Nb-, NbN-, NbC- and Nb₃Sn-surfaces *IEEE Transactions on Magnetics*, **23**(2) 1381 – 1384
55. Tyagi P V, Saeki T, Sawabe M, Hayano H and Kato S 2012 Study of HPR created oxide layers at Nb surfaces *Proceedings of LINAC2012 (Tel-Aviv, Israel)* 336-338
56. Smith J F, Carlson O N and De Avillez R R 1987 The Niobium carbon system *Journal of Nuclear Materials* **148** 1-16